Microstructural design and experimental validation of elastic metamaterial plates with anisotropic mass density

R. Zhu,[1] X. N. Liu,[1] G. L. Huang,[1,*] H. H. Huang,[2] and C. T. Sun[3]

[1]*Department of Systems Engineering, University of Arkansas at Little Rock, Little Rock, Arkansas 72204, USA*
[2]*Department of Engineering Science and Ocean Engineering, National Taiwan University, Taipei 10617, Taiwan*
[3]*School of Aeronautics and Astronautics, Purdue University, West Lafayette, Indiana 47907, USA*

A microstructure design of anisotropic resonant inclusions is investigated for the elastic metamaterial plate with the aid of the numerically based effective medium model. Experimental validation is then conducted in the anisotropic metamaterial plate through both harmonic and transient wave testing, from which the anisotropic effective dynamic mass density, group, and phase velocities are determined as functions of frequency. The strongly anisotropic mass density along two principal orientations is observed experimentally and the prediction from the experimental measurements agrees well with that from the numerical simulation. Finally, based on the numerically obtained effective dynamic properties, a continuum theory is developed to simulate different guided wave modes in the elastic metamaterial plate. Particularly, high-order guided wave coupling and repulsion as well as the preferential energy flow in the anisotropic elastic metamaterial plate are discussed.

I. INTRODUCTION

Recently, elastic metamaterials (EMMs) have gained much attention due to their potential to possess unique effective material properties while maintaining reasonable sample size. Because of the vector characteristics of elastic waves and the possible coupling between longitudinal and transverse modes, richer wave propagation phenomena are expected in the EMMs. Various novel concepts and engineering applications of EMMs have been successfully demonstrated, for example, mechanical filters, sound and vibration isolators, elastic waveguides, and energy harvesters.[1–7] Most of these approaches rely on resonant inclusions and the resulting EMM parameters vary strongly with frequency. In the previous work, the anisotropic effective mass density tensor of an EMM made of lead cylinders coated with elliptical rubber in an epoxy matrix was numerically determined.[8] However, its practical design and experimental validation have not yet been systematically investigated.

The quest for the anisotropic effective mass density of EMMs has been partly inspired by the success obtained from the acoustic metamaterials (AMMs), in which only the longitudinal wave mode exists. Cummer and Schurig[9] have numerically presented the possibility of acoustic cloaking by means of AMMs with the anisotropic mass density; however, engineering the AMM was still a challenge at the time. Based on Schoenberg and Sen's work,[10] Cheng *et al.*[11] designed an AMM with anisotropic mass density by using a concentric alternating homogeneous isotropic layered fluid. A feasible method to build and characterize fluidlike cylinders with cylindrically anisotropic mass density has been presented based on the idea that a corrugated structure with radial symmetry can be described by a fluid-fluid multilayered structure.[12] In addition, another new class of AMMs with a dynamical anisotropic effective mass density was numerically designed through two-dimensional anisotropic arrangements of full elastic cylinders embedded in a nonviscous fluid.[13] A similar anisotropic design was suggested in AMMs composed of perforated solid plates

in a fluidlike background.[14] Zigoneanu *et al.*[15] presented the experimental realization and characterization of an AMM with strongly anisotropic effective mass density. The metamaterial is composed of arrays of solid inclusions in a background of air, and the anisotropy is controlled by the rotational asymmetry of these inclusions. Most of these approaches do not rely on resonant inclusions; therefore, the resulting AMM anisotropic parameters vary strongly in a broad frequency range.

Different from AMMs, anisotropy of the effective mass density of EMMs can only be engineered by using anisotropic resonant inclusions instead of anisotropic lattices. Microstructure design of EMMs by embedding rubber-coated lead spheres in an epoxy matrix can be traced back to 2000.[1] The resulting band gap was later explained by negative effective mass density.[16] Milton and Willis[17] first proposed a two-dimensional (2D) spring-mass locally resonant model which shows that the effective mass density could become anisotropic. In order to fabricate the EMM with effective anisotropic mass density, Milton[18] suggested a soft-layer-coated elliptic lead core in the solid model, which is modified from the original model proposed by Sheng *et al.*[19] Gu *et al.*[20] investigated local resonance modes of elliptic cylinders coated with silicon rubber in a rigid matrix to obtain the anisotropic effective mass density. To explain the physical mechanism of the anisotropic mass density, a 2D lattice model that is composed of anisotropic resonators was studied analytically to obtain a second-order anisotropic effective mass density tensor.[21] However, few EMMs have been fabricated and demonstrated experimentally at structural levels because of the lack of systematic analysis of feasible microstructure designs.

In the paper, we expand upon the previous work[8] and demonstrate experimentally that relatively complex resonant inclusions in a solid plate can create a strongly anisotropic effective mass density. First, the numerically based effective method is employed to calculate the anisotropic effective mass density tensor of the EMM plate. Thus, a design of the EMM plate with strongly anisotropic mass density is proposed in the continuum manner. The experimental validation is

144307-1

then conducted on the proposed microstructure design of the EMM plate through both harmonic and transient wave testing. Strong anisotropy of the effective mass densities along two principal orientations is obtained and found to be in excellent agreement with the prediction of the numerical simulation. Specifically, the phase and group velocities of the EMM plate are experimentally determined through the transient elastic wave transmission measurements, and its effective dynamic mass density is experimentally determined from the measured phase velocity as a function of frequency. Finally, to analyze different wave modes in the EMM plate a continuum model of the EMM plate is developed, and the wave phenomena such as the wave coupling and repulsion as well as the preferential energy flow are discussed.

II. DESIGN OF EMMs WITH ANISOTROPIC EFFECTIVE MASS DENSITY

Knowing the effective dynamic properties of the EMM is a necessary condition for the microstructure design and its wave propagation characteristics. For isotropic EMMs, the three independent effective parameters can be determined: effective bulk modulus, effective shear modulus, and effective mass density.[22,23] For the EMM with simple microstructures, such as circular-coated spheres or cylinders, analytically based effective medium theories have been developed.[16,24] However, in order to design such artificial materials for the desired properties such as anisotropic effective mass density, EMMs must have complex microstructures. For the EMM with general complex microstructures, a numerically based effective medium model has been recently proposed to determine the effective dynamic properties based on the micromechanics approach.[8,25] A similar numerical approach was also suggested for EMMs with multiresonator systems.[26,27] In this section, the numerically based effective medium model is adopted for determination of the anisotropic effective mass density of the EMM and its microstructure design.

A. The numerically based effective medium model

In this subsection, the numerically based effective medium model is briefly reviewed. Figure 1 shows a representative volume element (RVE) of the three-dimensional (3D) EMM, in which the general soft-coated elastic core is embedded in the matrix. The lattice size is denoted as a. The key of this method

Lattice Cell of EMM   Continuum RVE

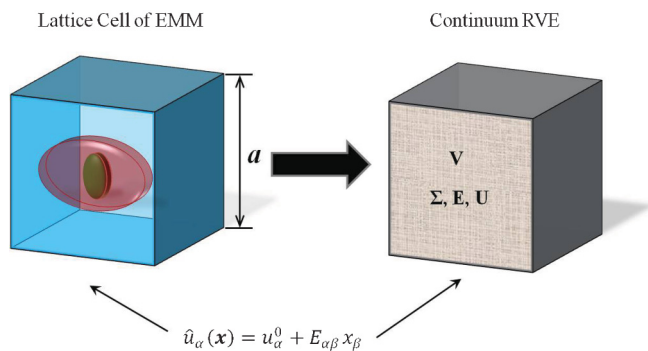$$\hat{u}_\alpha(\boldsymbol{x}) = u_\alpha^0 + E_{\alpha\beta} x_\beta$$

FIG. 1. (Color online) Representation of EMM lattice cell with arbitrary microstructure by a homogeneous solid.

is to replace the EMM with an equivalent continuous medium under dynamic harmonic loadings. At the macroscopic scale, it is assumed that the composite material will behave as the medium under the applied global deformation. The difficulty of the numerical study is that most standard finite-element software does not have a feature to directly deal with the problem with complex variables in the harmonic analysis. This difficulty can be overcome by solving problems with real and imaginary parts of the constraint conditions separately.[25]

The applied local displacement on the boundary of the unit cell can be described as

$$u_\alpha(x,t) = \hat{u}_\alpha(x)e^{i\omega t}, \tag{1}$$

where $\hat{u}_\alpha(x) = u_\alpha^0 + E_{\alpha\beta}x_\beta (\alpha,\beta = 1,2,3)$, and $\hat{u}_\alpha$ is the displacement field compatible with a preassumed macrostrain $E_{\alpha\beta}$ plus a rigid translation u_α^0; x_β is the local position vector in the unit cell. The effective medium parameters can then be calculated considering the boundary response of the metamaterial unit cell that "feels" and "responds to" the stimulation exerted by the outside elastic waves. Under the long-wavelength assumption, the effective stress, strain, resultant force, and acceleration of the unit cell with the complex microstructure can be obtained by averaging local quantities on the external boundary as

$$\Sigma_{\alpha\beta} = \frac{1}{V}\int_{\partial V}\sigma_{\alpha\gamma}x_\beta ds_\gamma, \quad E_{\alpha\beta} = \frac{1}{2V}\int_{\partial V}(u_\alpha ds_\beta + u_\beta ds_\alpha),$$

$$F_\alpha = \frac{1}{V}\int_{\partial V}\sigma_{\alpha\beta}ds_\beta, \quad \ddot{U}_\alpha = \frac{1}{S}\int_{\partial V}\ddot{u}_\alpha ds, \tag{2}$$

where $\sigma_{\alpha\beta}$, u_α, and $\ddot{u}_\alpha$ are the local stress, displacement, and acceleration fields, respectively, $ds_\alpha = n_\alpha ds$ with n_α being the boundary unit normal, V and ∂V denote unit cell's volume and external boundary. Specifically, the anisotropic effective mass density of the EMM can be determined based on the following relation:

$$\begin{bmatrix} F_1 \\ F_2 \\ F_3 \end{bmatrix} = -\omega^2 V \begin{bmatrix} \rho_{11} & \rho_{12} & \rho_{13} \\ \rho_{12} & \rho_{22} & \rho_{23} \\ \rho_{13} & \rho_{23} & \rho_{33} \end{bmatrix} \begin{bmatrix} \hat{U}_1 \\ \hat{U}_2 \\ \hat{U}_3 \end{bmatrix}, \tag{3}$$

where $\hat{U}_\alpha$ is the global displacement field. For example, to calculate the anisotropic effective mass density components ρ_{11}, ρ_{12}, and ρ_{13}, the dynamic displacement constraints on the boundary of the RVE are applied as $\hat{U}_1 = Ae^{iwt}$ and $\hat{U}_2 = \hat{U}_3 = 0$. In the principal coordinate system, we have $\rho_{\alpha\beta} = 0$ when $\alpha \neq \beta$. For arbitrary x-y-z coordinate system, it can be numerically proved that the in-plane (x-y plane) anisotropic effective mass density follows the coordinate transformation law as

$$\begin{bmatrix} \rho_{xx} & \rho_{xy} & \rho_{xz} \\ \rho_{xy} & \rho_{yy} & \rho_{yz} \\ \rho_{xz} & \rho_{yz} & \rho_{zz} \end{bmatrix} = \begin{bmatrix} C & S & 0 \\ -S & C & 0 \\ 0 & 0 & 1 \end{bmatrix} \begin{bmatrix} \rho_{11} & 0 & 0 \\ 0 & \rho_{22} & 0 \\ 0 & 0 & \rho_{33} \end{bmatrix}$$

$$\times \begin{bmatrix} C & S & 0 \\ -S & C & 0 \\ 0 & 0 & 1 \end{bmatrix}^{-1}, \tag{4}$$

where $C = \cos\delta$, $S = \sin\delta$, δ is the angle between the x axis in the arbitrary coordinate system and the x_1 axis in the principal coordinate system. Therefore, the effective mass density admits the second-order tensorial property. For
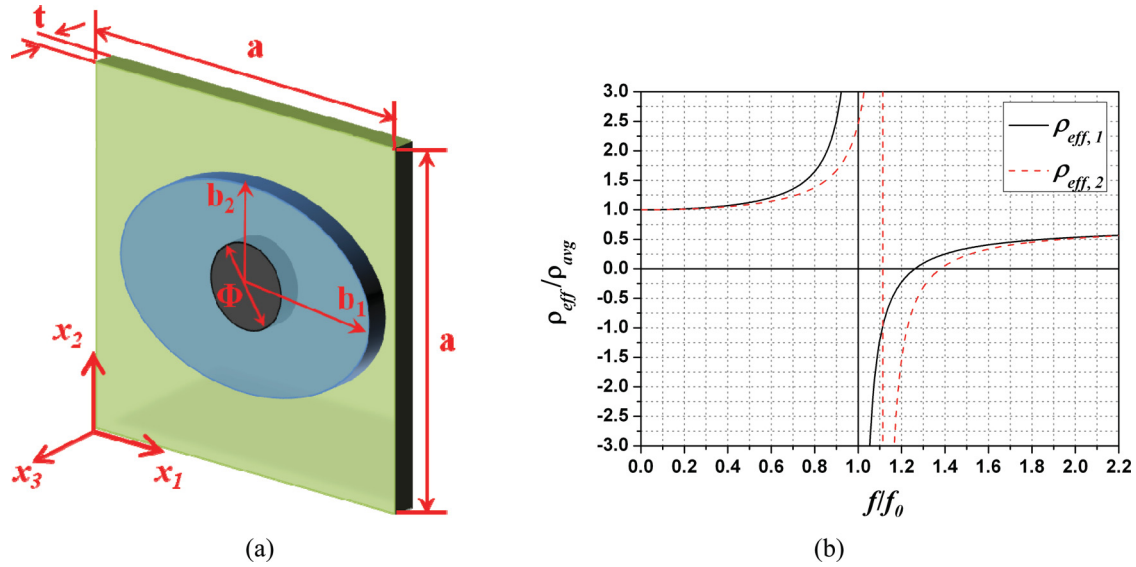
FIG. 2. (Color online) (a) Unit cell of the EMM plate with elliptical coating layer. (b) Normalized effective mass densities as functions of the normalized frequency along different principal directions.

the determination of the effective moduli of the EMM, the anisotropic moduli can be similarly obtained based on the constitutive relations. For example, for a 2D orthogonal EMM, the stiffness tensor can be simplified as only four effective parameters. After obtaining the three effective stresses and three effective strains on the boundary, the effective stiffness parameters can be calculated from the constitutive relations.

B. Design of the EMM plate with anisotropic dynamic mass density

The working mechanism of the EMM with anisotropic effective mass density is fully dependent on the inner microstructure design, which was clearly explained by analyzing the 2D mass-in-mass lattice model.[21] Based on the mass-in-mass system, the effective mass densities along the two principal directions can be analytically expressed as

$$\rho_{eff,1} = \frac{1}{V}\left(m_1 + \frac{\omega_{0,1}^2}{\omega_{0,1}^2 - \omega^2}m_2\right), \tag{5}$$

$$\rho_{eff,2} = \frac{1}{V}\left(m_1 + \frac{\omega_{0,2}^2}{\omega_{0,2}^2 - \omega^2}m_2\right), \tag{6}$$

where V is the volume of the unit cell, m_1 and m_2 are outer and inner masses, respectively, and $\omega_{0,1} = \sqrt{k_1/m_2}$ and $\omega_{0,2} = \sqrt{k_2/m_2}$ are the locally resonant frequencies of the inner mass along the x_1 and x_2 directions, respectively. From

Eqs. (5) and (6), it can be found that the anisotropy between $\rho_{eff,1}$ and $\rho_{eff,2}$ is mainly caused by the difference between the locally resonant frequencies $\omega_{0,1}$ and $\omega_{0,2}$, which can be tuned through the design of the internal springs k_1 and k_2 along the x_1 and x_2 directions, respectively. Specifically, design of the local stiffness anisotropy in the coating layer is the key to achieving the anisotropic effective mass density of the EMM. In this study, efforts on the microstructure design of the EMM plate with in-plane anisotropic effective mass density will be focused on modification of the well-known three-component sonic crystal, soft-layer-coated heavy core embedded in a matrix. A coating layer with an elliptical shape is suggested to achieve the anisotropic effective mass density of the EMM plate with the x_3 axis normal to the plate and the in-plane x_1 and x_2 axes are parallel to the elliptical semimajor axis and the semiminor axis, respectively, as shown in Fig. 2(a). The microstructure geometrical and constituent material parameters are given in Table I.

The normalized effective mass densities along the x_1 and x_2 directions as functions of the normalized frequency are calculated based on the numerically based effective medium model, which is shown in Fig. 2(b). In the figure, ρ_{avg} is the average static mass density for the composite and f_0 is the locally resonant frequency of the microstructure along the x_1 direction. It is noticed that $\rho_{eff,1}$ and $\rho_{eff,2}$ have different values in the normalized frequency range from $f/f_0 = 0.4$ to $f/f_0 = 1.8$. However, the anisotropic design is quite limited to the ratio

TABLE I. Microstructure geometrical and material parameters.

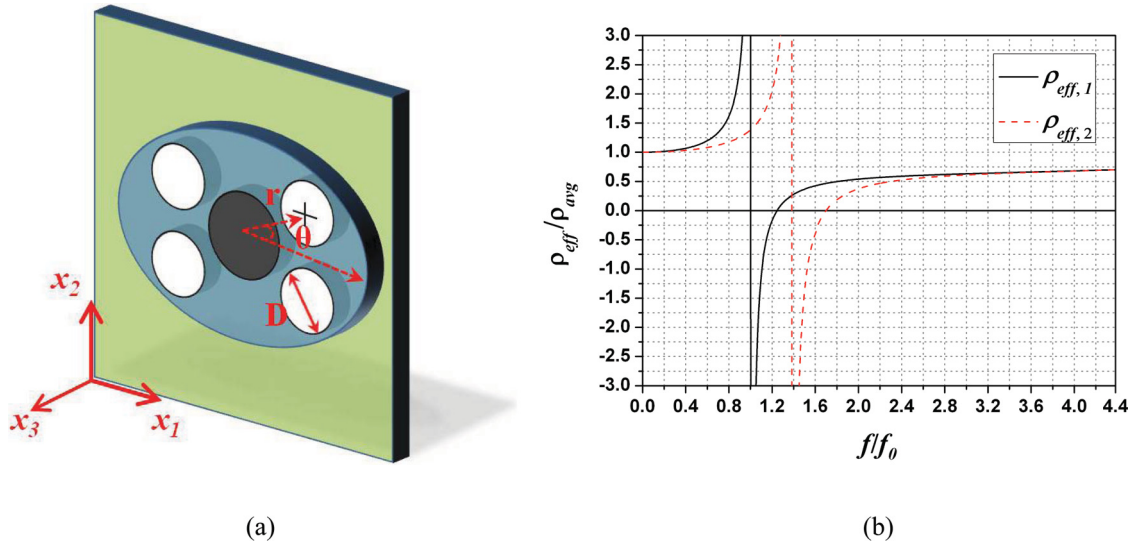| Geometrical parameters			Material parameters		
			Matrix: Aluminum	Coating: Epoxy	Core: Lead
a	11 mm				
b_1	4.95 mm	Mass density	2700 kg/m³	1033 kg/m³	11 310 kg/m³
b_2	3.5 mm	Young's modulus	71 GPa	0.595 GPa	13 GPa
Φ	3.175 mm	Poisson's ratio	0.32	0.38	0.435
t	3.175 mm				

(a)

(b)

FIG. 3. (Color online) (a) Unit cell of the EMM plate with micropores in the coating layer. (b) Normalized effective mass densities as functions of the normalized frequency along different principal directions.

of the semimajor axis to the semiminor axis of the coating ellipse. To achieve a more strongly anisotropic effective mass density, a more modified microstructure design is needed.

Figure 3(a) shows a microstructure design in the elliptical coating layer with four symmetric micropores for the greater anisotropy in mass density. The same geometrical and material parameters in Table I are used. The diameter of the micropore is $D = 2.15$ mm and the centers of the four symmetric micropores are located at $r = 3.13$ mm with the orientation angles (θ) being 25°, 155°, 205°, and 335°, respectively. Figure 3(b) shows the in-plane normalized effective mass density of the EMM plate with the micro-pores as a function of the normalized frequency. Comparing with the results in Fig. 2(b), it can be observed that the lower-frequency band of the of $\rho_{eff,1}$ and $\rho_{eff,2}$ stays the same; however, the upper band is dramatically increased from $f/f_0 = 1.8$ to $f/f_0 = 3.0$, which shows that stronger anisotropy of the effective mass density can be achieved through the current microstructure design. The same lower-frequency band is expected because of the frequency normalization with respect to the static average mass density. It is also interesting to note that the effective mass density becomes isotropic ($\rho_{eff,1} = \rho_{eff,2}$) when the frequency is close to the static case or much larger than the resonant frequencies. The different constant values of the effective mass density in static ($f/f_0 < 0.1$) and high-frequency ($f/f_0 > 4.0$) cases can be explained by Eqs. (5) and (6). It should be mentioned that the anisotropy can be further tuned through the change of the positions, shapes, and sizes of the micropores in the coating layer and the inner mass.

III. EXPERIEMENTAL VALIDATION

The experimental testing was conducted on the proposed microstructure design of the EMM plate in Fig. 3(a). The EMM plates were manufactured with the aid of a computer numerical control (CNC) machine. First, the tests of the harmonic lowest symmetric guided waves along the two in-plane principal directions were performed to demonstrate

different band gaps due to the anisotropic effective mass density of the EMM plate. The group and phase velocity dispersion relations were experimentally determined from measurements of the transmitted transient wave signals with the aid of the wavelet technology, from which the anisotropic effective mass densities of the EMM plate along the principal directions were obtained.

A. The experimental setup

Two anisotropic EMM plates with the proposed microstructure pattern were manufactured for the guided wave propagation tests along the two principal directions. Figure 4 schematically shows the fabrication procedure of the EMM plate. First, elliptical holes in a rectangular array (10×3) were drilled in the host aluminum (Al) plate (Type 6061)
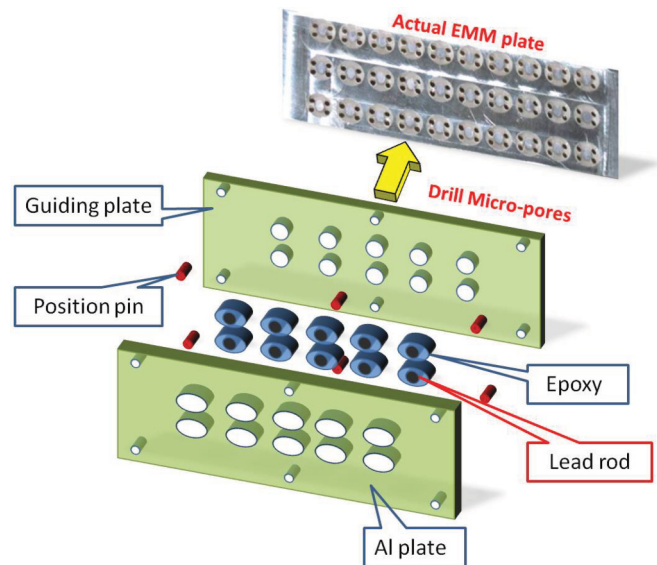

FIG. 4. (Color online) Schematic diagram of the EMM plate fabrication.
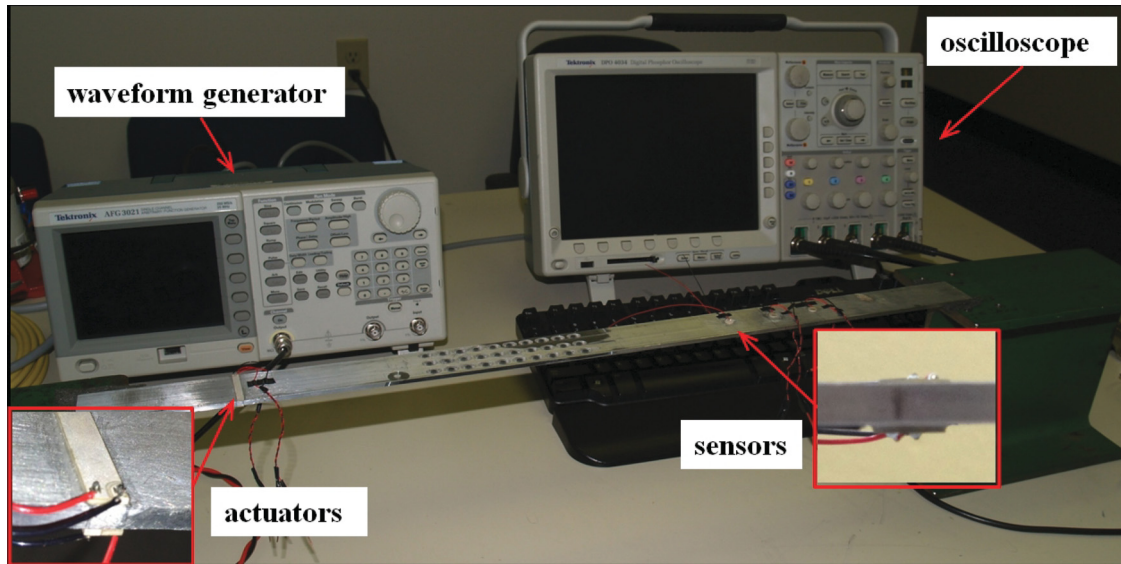
FIG. 5. (Color online) The experimental setup for harmonic testing of guided wave propagation in the EMM plate.

using the CNC machine. Second, pure lead rods (ESPI Metals) and liquid epoxy (Crystal Clear 202, Smooth-On, Inc.) were implanted into the holes. A guiding plate was used to precisely locate the lead rods. After curing, micropores in the epoxy coating were formed with the CNC machine. The material properties of the Al plate, cured epoxy, and the lead rods are listed in Table I. The epoxy properties were measured by the simple tension testing of the epoxy samples.

To qualitatively investigate the anisotropic dynamic behavior of the EMM plate, the transmission characterizations of the lowest symmetric guided waves propagating in the EMM plates along the two principal directions were first performed experimentally. The experimental setup, shown in Fig. 5, includes the following components: (1) arbitrary waveform generator (Tektronix AFG 3021) and power amplifier (Krohn-Hite 7602M); (2) two symmetrically surface-bonded rectangular piezoelectric actuators (P-33.00 mm-4.00 mm-0.76 mm-850 WFB, APC International, Ltd), as shown in the left inset. The same voltage input is applied on the two actuators to generate the harmonic lowest symmetric guided wave; (3) two circular piezoelectric disks (P-6.36 mm-0.76 mm-850, WFB, APC International, LTD), as shown in the right inset, which are symmetrically surface bonded on the other side of the EMM plate and function as sensors; (4) a digital data acquisition system including a digital oscilloscope (Tektronix DPO4034) and a personal computer for the measurement, storage, and analysis of the received sensor signals. By using the summation of the outputs of both sensors, we can get a purely symmetric guided wave signal and efficiently eliminate the unwanted asymmetric wave signal which may come from the slight position mismatch of the two actuators.

B. Wave transmission measurements

Harmonic wave analysis was performed, and the transmitted wave signal of the EMM plate at each harmonic frequency was measured and recorded. By sweeping the frequency of the input harmonic signal, transmitted signals in the frequency regime of interest can be secured. Figure 6 shows the lowest

symmetric guided wave transmission of the EMM plates along the two principal directions. For validation purposes, the transmission results of the infinite EMM plates predicted by the numerical simulations are compared with the experimental results. For wave propagation along x_1 direction, a wave band gap can be found at the frequency range from 18.2 to 21.8 kHz; however, the wave band gap is found at the frequency range from 24.8 to 30.4 kHz for wave propagation along the x_2 direction. For the current microstructure design, the observed band gaps can be explained by the negative effective mass density.[16] Therefore, the strong anisotropy of the effective mass density is clearly revealed through the difference of the experimentally measured band gaps along different wave propagation directions. Very good agreements between the experimental measurement and the numerical prediction also validate the experimental testing.

C. Experimental determination of the effective mass density

The effective mass density of the EMM has been analyzed numerically and analytically by numerous methods. However, to the best of our knowledge, experimental determination of the effective mass density of the EMM plate as a function of frequency has not yet been investigated. In order to do that, a transient wave propagation testing in the EMM plate should be conducted to find the group and phase velocities instead of the harmonic wave testing. The main difficulty of the transient wave testing in the solid EMM plate is the wave signal complexity due to the interference by the reflected waves from the two free ends. In this study, the boundary reflection was eliminated by welding two extended Al plates with the same width and thickness to both ends of the EMM plate. In the experiment, the group and phase velocities cannot be obtained directly from $c_g = \frac{d\omega}{dk}$ and $c_p = \frac{\omega}{k}$, because the time origins of the practical collected signals are simultaneously delayed to the time when the physical waves were excited. Moreover, not all frequency components appear at the same time; a so-called "time lag" exists between different frequency components.
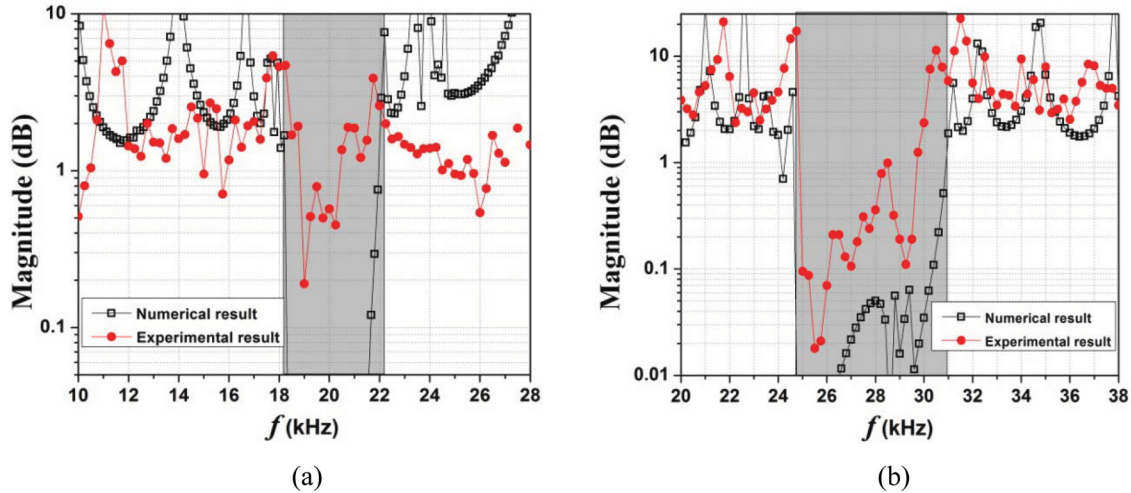
FIG. 6. (Color online) Comparisons of numerical and experimental transmission measurements of the lowest symmetric guided wave propagation in the anisotropic EMM plate along (a) x_1 direction and (b) x_2 direction. The shaded regions indicate the corresponding band gaps predicted by the numerical simulations.

Therefore, using two sensors to measure the response waves at the same time can effectively eliminate these side effects. In the study, two symmetrically bonded piezoelectric sensor pairs on both sides of the EMM plate were used to receive the transient wave signals, as shown in Fig. 7. In the figure, $d = 225$ mm is the distance between two sensor pairs and $d_0 = 110$ mm is the length of the EMM.

A tune-burst broadband wave signal with the mathematical expression of $V(t) = A_0[1 - \cos(2\pi f_c t)]\sin(2\pi f_c t)$ was chosen, where A_0 is the amplitude and f_c is the central frequency. Different central frequencies in the passing band were selected to cover the frequency regime of interest. Figure 8 shows the received sensor signals before and after the EMM plate shown in Fig. 7 at the central frequency $f_c = 13.6$ kHz, which is within the frequency regime of the passing band. As shown in Fig. 8(a), the sensor signal collected from sensor pair 1 is the direct propagating wave signal followed by the strongly reflected wave from the heterogeneous EMM plate. The significant wave dispersion can be found in the transmitted signal collected from sensor pair 2, as shown in Fig. 8(b), which makes it very difficult to interpret directly.

1. Determination of group velocity

The continuous wavelet transform (CWT) based on the Gabor wavelets, which has been demonstrated as a useful time-frequency analysis tool of wave signals in structural health monitoring (SHM),[28] is used to obtain the group and phase velocity dispersion curves of the EMM plate. The CWT of a given signal $s(t)$ can be mathematically expressed as follows:

$$WT(\hat{a},\hat{b}) = \frac{1}{\sqrt{\hat{a}}} \int_{-\infty}^{+\infty} s(t)\overline{\psi\left(\frac{t - \hat{b}}{\hat{a}}\right)}dt, \qquad (7)$$

where $\psi(t)$ is the mother wavelet function and the overline indicates the complex conjugate; $\hat{a}$ and $\hat{b}$ are known as the scale and translation parameters, respectively. The reciprocal of $\hat{a}$ is associated with the frequency and $\hat{b}$ is related to the time. The Gabor function is chosen as the mother wavelet function in the analysis since it can provide better resolutions both in the time and frequency domains than any other wavelets. The Gabor function is expressed as[29]

$$\psi(t) = \frac{1}{\sqrt[4]{\pi}} \sqrt{\frac{\hat{\omega}_0}{\gamma}} \exp\left[-\frac{(\hat{\omega}_0/\gamma)^2}{2}t^2\right]\exp\left(i\hat{\omega}_0 t\right), \qquad (8)$$

where γ and $\hat{\omega}_0$ are positive constants chosen as $\pi\sqrt{2/ln2} \approx 5.336$ and 2π, respectively. The Gabor function may be considered as a Gaussian window function centered at $t = 0$ and its Fourier transform centered at $\omega = \hat{\omega}_0$. Therefore, the CWT using the Gabor wavelet represents the time-frequency component of $s(t)$ around time $t = \hat{b}$ and frequency $\omega = \hat{\omega}_0/\hat{a}$. For example, Figs. 9(a) and 9(b) show the 2D plots of the magnitudes of CWT coefficients of the measured sensor
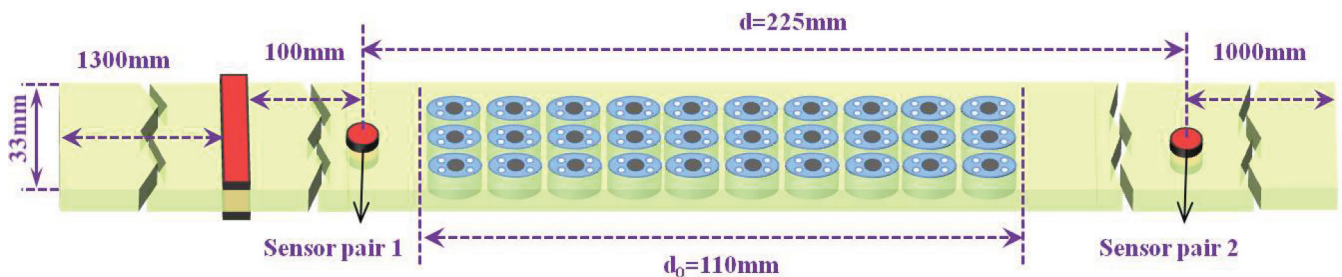

FIG. 7. (Color online) Schematic diagram of the experimental setup for the group and phase velocity determinations in the EMM plate.
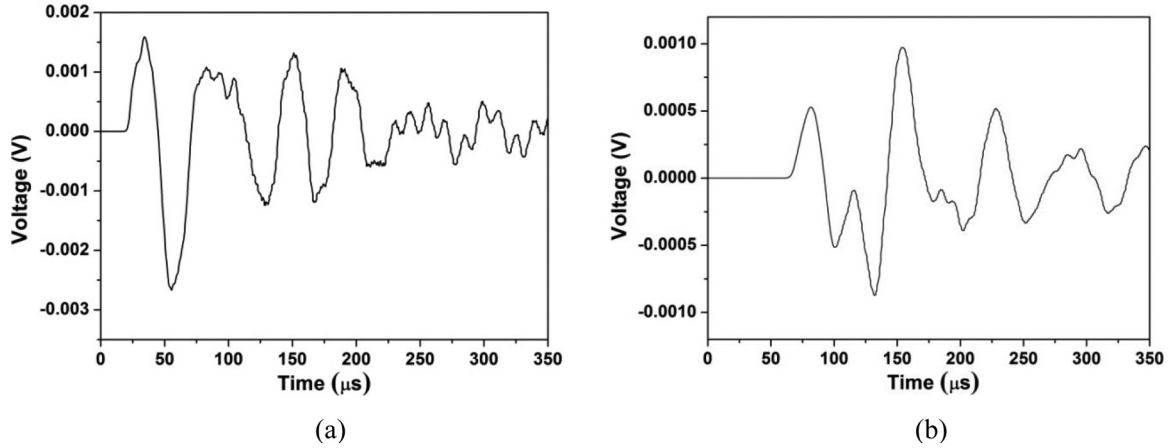
(a)

(b)

FIG. 8. The transient wave signals collected from (a) sensor pair 1 and (b) sensor pair 2 at the central frequency $f_c = 13.6$ kHz.

signals in Figs. 8(a) and 8(b), respectively, for a scale with the central frequency $f_c = 13.6$ kHz. Physically, the magnitude of CWT reaches its maximum at the wavelet ridge point; the corresponding time $\hat{b}$ of the ridge point is the group delay which equals the delay of the propagating wave signal envelope; therefore, it can be used in the calculation of the dispersive group velocity at the frequency. The group delays at the two sensor pairs at the frequency are determined by the peak locations of the magnitudes of CWT coefficients of the sensor signals. The difference in the group delays of the waves at two sensor pairs, Δt, is then obtained for the group velocity calculation without side effects.

In the current sensor deployment, the group velocity as a function of frequency can then be determined with the change of scale as

$$C_g(f) = d_0 \left/ \left[\Delta t(f) - \frac{d - d_0}{C_g^M} \right] \right. , \qquad (9)$$

where $C_g^M = 5400$ m/s is the group velocity in the host Al plate. Figure 10 shows the measured group velocity of the lowest symmetric guided wave mode in the EMM plate along

the x_1 direction. For comparison, the group velocity calculated from the theoretical analysis via the relationship $c_g = \frac{d\omega}{dk}$ is also plotted in the figure. The geometrical and material properties used in the calculation are listed in Table I. Good agreement between the theoretical result and the experimental measurement can be found in both the first and second passing bands.

2. Determination of phase velocity and effective mass density

Determination of the phase velocity of the EMM plate needs the information of the phase angle of the CWT coefficient. At a given scale $\hat{a}$ (frequency), the phase angle of the sensor signal corresponding to certain group delay $\hat{b}$ can be directly determined from the complex CWT coefficient as $\phi(\hat{a}, \hat{b})$, which is in the range of $-\pi$ to π. In order to calculate the exact phase difference $\Delta\phi$ between the two sensor signals, the branch number m of the inverse trigonometric function needs to be considered. By using the continuity of the phase spectrum, the proper branch number for each scale can be selected; therefore $\Delta\phi$ can be determined at each frequency. Finally the phase velocity of the EMM plate as a function of
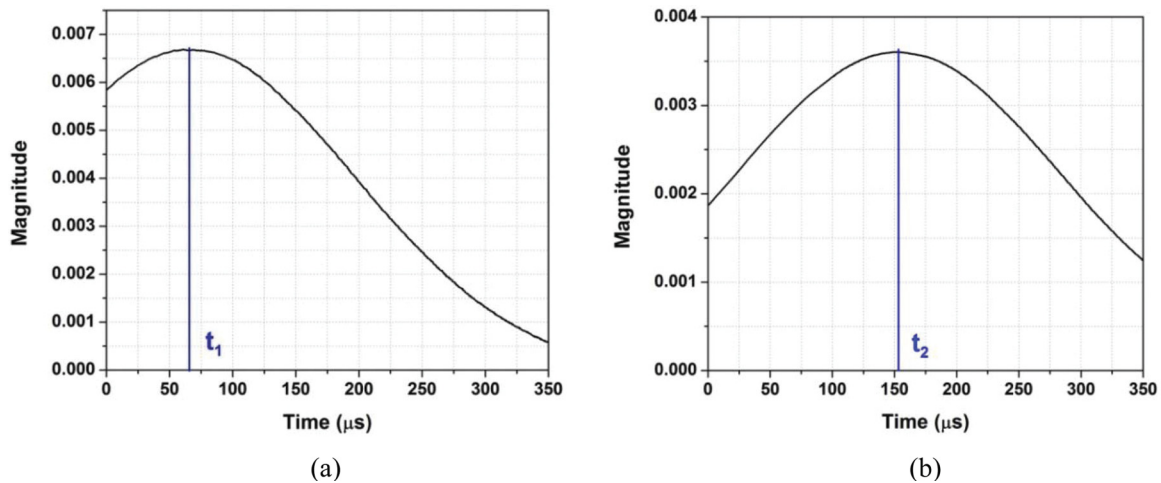

(a)

(b)

FIG. 9. (Color online) The magnitudes of CWT coefficients of the sensor signals collected from (a) sensor pair 1 and (b) sensor pair 2 at $f_c = 13.6$ kHz.
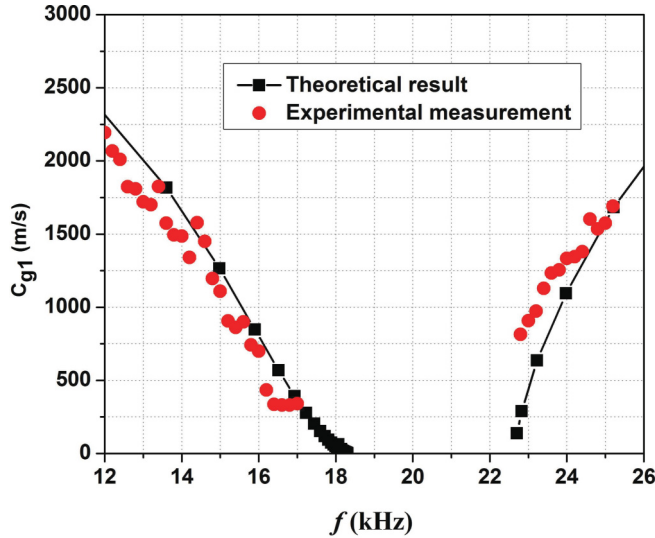
FIG. 10. (Color online) Experimentally measured group velocity of the lowest symmetric guided wave mode along the x_1 direction as a function of frequency.

frequency can be obtained using the following relation:

$$C_p(f) = \frac{d_0}{\left[\Delta t(f) + \frac{\Delta \phi(f)}{2\pi f} - \frac{d - d_0}{C_p^M} \right]}, \quad (10)$$

where Δt is the difference of the arrival time, and C_p^M is the phase velocity in the host plate. With the change of scale, the dispersive phase velocity versus the frequency can be finally obtained. Figure 11 shows the phase velocity of the EMM plate from the measured sensor signals. For comparison, the phase velocity predicted from the theoretical dispersion relation of the EMM plate is also added. In general, the measured phase velocity matches well with that from the theoretical prediction in the frequency range of the two lowest passing bands. Good agreement can be found in the frequency range of weak dispersion; however, a small discrepancy can be observed in
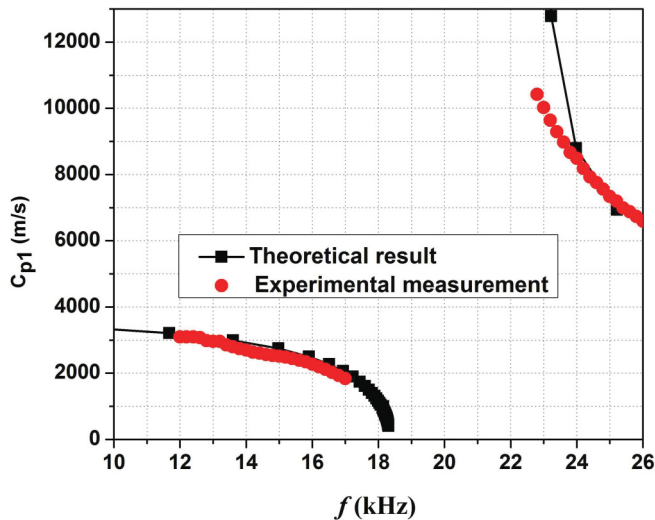

FIG. 11. (Color online) Experimentally measured phase velocity of the lowest symmetric guided wave mode along the x_1 direction as a function of frequency.

the range of strong dispersion, such as the frequency range close to the band gap.

Finally, the anisotropic effective mass density of the EMM plate can be determined by the experimentally measured phase velocity and the effective stiffness predicted by the numerically based effective medium model. For example, for the lowest symmetric guided wave propagating along the principal x_1 direction, the effective mass density of the EMM plate along the wave propagating direction can be determined by $\rho_1(f) = C_{11}^{eff}/[C_{p1}(f)]^2$. Figure 12 shows the obtained effective mass densities as functions of the frequency for wave propagation along two principal directions based on the experimental data. For comparison, the corresponding effective mass densities from the numerical solutions are also plotted. Excellent agreement can be observed even for the frequency range with strong wave dispersion. It should be noticed that the distribution of the locally resonant elements in the EMM plate will not affect its effective dynamic mass density, which is different from the AMM, because the anisotropic effective mass density of the EMM plate is mainly caused by the anisotropic resonant motion of the locally resonant element.

IV. CONTINUUM MODELING OF THE EMM PLATE

The dynamic behavior presented in the previous sections can be further modeled by using analytical approaches which provide more insight into the behavior of the system when undergoing internal resonance. The investigation developed here aims at developing an effective continuum model for different guided wave modes in the EMM plate, which are difficult to measure experimentally. The analytical results are compared with the experimental measurements and the numerical simulations in different EMM plates. Some interesting dynamic phenomena will be discussed such as high-order guided wave coupling and repulsion in the anisotropic EMM plate. The developed effective continuum model can be applied to problems of time-dependent vibration and transient wave propagation in the EMM plate, which is important for its potential engineering applications.

In general, based on the numerically determined effective stiffness, the 3D stress-strain relation of the EMM plate in the principal coordinate system can be expressed as

$$\begin{Bmatrix} \sigma_{11} \\ \sigma_{22} \\ \sigma_{33} \\ \tau_{23} \\ \tau_{13} \\ \tau_{12} \end{Bmatrix} = \begin{bmatrix} C_{11} & C_{12} & C_{13} & 0 & 0 & 0 \\ C_{12} & C_{22} & C_{23} & 0 & 0 & 0 \\ C_{13} & C_{23} & C_{33} & 0 & 0 & 0 \\ 0 & 0 & 0 & C_{44} & 0 & 0 \\ 0 & 0 & 0 & 0 & C_{55} & 0 \\ 0 & 0 & 0 & 0 & 0 & C_{66} \end{bmatrix} \begin{Bmatrix} \varepsilon_{11} \\ \varepsilon_{22} \\ \varepsilon_{33} \\ \gamma_{23} \\ \gamma_{13} \\ \gamma_{12} \end{Bmatrix}. \quad (11)$$

In an arbitrary x-y-z coordinate system (in-plane: x-y plane, out-of-plane: z axis), the constitutive equations can be derived using coordinate transformation and written as

$$\begin{Bmatrix} \sigma_x \\ \sigma_y \\ \sigma_z \\ \tau_{yz} \\ \tau_{xz} \\ \tau_{xy} \end{Bmatrix} = [\bar{C}_{ij}] \begin{Bmatrix} \varepsilon_x \\ \varepsilon_y \\ \varepsilon_z \\ \gamma_{yz} \\ \gamma_{xz} \\ \gamma_{xy} \end{Bmatrix}, \quad (12)$$
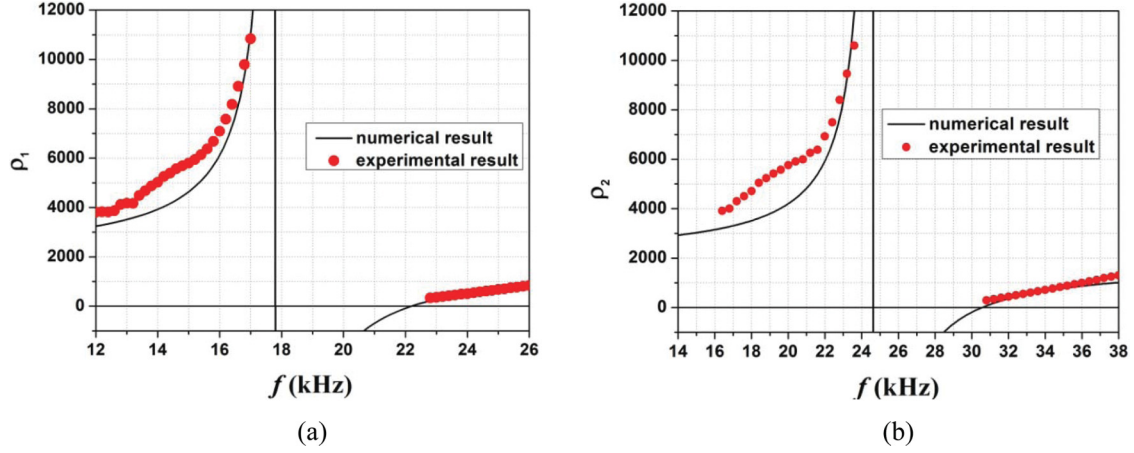
FIG. 12. (Color online) Effective dynamic mass densities of the anisotropic EMM plate along the two principal directions: (a) x_1 direction; (b) x_2 direction.

where $\bar{C}_{ij}$, $i,j = 1$ to 6, are the transformed elastic constants. The equations of motion for the continuum plate with anisotropic mass density tensor can be written as

$$\sigma_{x,x} + \tau_{xy,y} + \tau_{xz,z} = \rho_{xx}\ddot{u} + \rho_{xy}\ddot{v} + \rho_{xz}\ddot{w},$$
$$\tau_{xy,x} + \sigma_{y,y} + \tau_{yz,z} = \rho_{xy}\ddot{u} + \rho_{yy}\ddot{v} + \rho_{yz}\ddot{w}, \quad (13)$$
$$\tau_{xz,x} + \tau_{yz,y} + \sigma_{z,z} = \rho_{xz}\ddot{u} + \rho_{yz}\ddot{v} + \rho_{zz}\ddot{w}.$$

For the proposed metamaterial plate, the traction-free boundary conditions on the top and bottom surfaces are

$$\sigma_z = \tau_{xz} = \tau_{yz} = 0, \quad z = \pm h/2. \quad (14)$$

For a guided wave along the x direction, the displacements can be assumed as the form

$$u = Ae^{ikpz}e^{i[k_x x - \omega t]}, \quad v = Be^{ikpz}e^{i[k_x x - \omega t]},$$
$$w = Ce^{ikpz}e^{i[k_x x - \omega t]}, \quad (15)$$

where $k_x = \frac{\omega}{c_p}$ is the wave number, ω is the angular frequency, c_p is the phase velocity, and p is an unknown variable to be determined. Substituting Eqs. (12) and (15) into Eq. (13), we have the following matrix form:

$$\begin{bmatrix} \Gamma_{11} & \Gamma_{12} & \Gamma_{13} \\ \Gamma_{12} & \Gamma_{22} & \Gamma_{23} \\ \Gamma_{13} & \Gamma_{23} & \Gamma_{33} \end{bmatrix} \begin{Bmatrix} A \\ B \\ C \end{Bmatrix} = 0, \quad (16)$$

where

$$\Gamma_{11} = \bar{C}_{11} + \bar{C}_{55}p^2 - \rho_{xx}c_p^2,$$
$$\Gamma_{12} = \bar{C}_{16} + \bar{C}_{45}p^2 - \rho_{xy}c_p^2,$$
$$\Gamma_{13} = (\bar{C}_{13} + \bar{C}_{55})p - \rho_{xz}c_p^2,$$
$$\Gamma_{22} = \bar{C}_{66} + \bar{C}_{44}p^2 - \rho_{yy}c_p^2,$$
$$\Gamma_{23} = (\bar{C}_{36} + \bar{C}_{45})p - \rho_{yz}c_p^2,$$
$$\Gamma_{33} = \bar{C}_{55} + \bar{C}_{33}p^2 - \rho_{zz}c_p^2.$$

In order to obtain a nontrivial solution of Eq. (16), the following sixth-order polynomial needs to be satisfied:

$$p^6 + \alpha_1 p^4 + \alpha_2 p^2 + \alpha_3 = 0, \quad (17)$$

where $\alpha_l (l = 1,2,3)$ are functions of the stiffness matrix $\bar{C}_{ij}(i,j = 1$ to 6), the effective mass density $\rho_{rs}(r,s = x,y,z)$, and the phase velocity c_p.

By solving Eq. (17), the displacements can take the following summation forms as

$$u = \left(\sum_{j=1}^{6} A_j e^{ikp_j z} \right) e^{i[k_x x - \omega t]},$$
$$v = \left(\sum_{j=1}^{6} B_j e^{ikp_j z} \right) e^{i[k_x x - \omega t]}, \quad (18)$$
$$w = \left(\sum_{j=1}^{6} C_j e^{ikp_j z} \right) e^{i[k_x x - \omega t]},$$

where for each p_j ($j = 1$ to 6),

$$B = RA, R = \frac{\Gamma_{11}\Gamma_{23} - \Gamma_{12}\Gamma_{13}}{\Gamma_{13}\Gamma_{22} - \Gamma_{12}\Gamma_{23}},$$
$$C = SA, S = \frac{\Gamma_{11}\Gamma_{23} - \Gamma_{12}\Gamma_{13}}{\Gamma_{12}\Gamma_{33} - \Gamma_{23}\Gamma_{13}}.$$

Substituting Eq. (18) into Eq. (14), we have

$$\sum_{j=1}^{6} (H_{1j}, H_{2j}, H_{3j}) A_j e^{\pm ikp_j h/2} = 0, \quad (19)$$

where

$$H_{1j} = \bar{C}_{13} + \bar{C}_{33}p_j S_j + \bar{C}_{36}R_j,$$
$$H_{2j} = \bar{C}_{44}p_j R_j + \bar{C}_{45}(p_j + S_j),$$
$$H_{3j} = \bar{C}_{45}p_j R_j + \bar{C}_{55}(p_j + S_j).$$

The existence of a nontrivial solution of Eq. (19) leads to two independent dispersion relations:

$$H_{11}(H_{23}H_{35} - H_{25}H_{33})\cot\left(\frac{kp_1h}{2}\right) + H_{13}(H_{25}H_{31}$$

$$- H_{21}H_{35})\cot\left(\frac{kp_3h}{2}\right) + H_{15}(H_{21}H_{33} - H_{23}H_{31})$$

$$\times \cot\left(\frac{kp_5h}{2}\right) = 0, \qquad (20)$$

$$H_{11}(H_{23}H_{35} - H_{25}H_{33})\tan\left(\frac{kp_1h}{2}\right) + H_{13}(H_{25}H_{31}$$

$$- H_{21}H_{35})\tan\left(\frac{kp_3h}{2}\right) + H_{15}(H_{21}H_{33} - H_{23}H_{31})$$

$$\times \tan\left(\frac{kp_5h}{2}\right) = 0, \qquad (21)$$

which correspond to symmetric and antisymmetric wave modes, respectively.

To validate the continuum model, dispersion relations obtained from the current model will be compared with those from the FE simulation based on the detailed microstructures. We consider the EMM plate with the unit cell shown in Fig. 3(a). In the first example, the microstructure geometrical and material parameters are given in Table I and wave propagation along the principal x_1 direction is considered. The effective stiffness matrix of the EMM plate can be obtained by using the numerically based effective medium model, which is listed in Table II.

Figure 13 shows the dispersion relation in the first Brillouin zone of guided wave propagation along the principal x_1 direction in the EMM plate obtained from the continuum model, which includes the lowest symmetric (S_0) and antisymmetric (A_0) guided wave modes and shear horizontal (SH_0) wave mode. For comparison, the dispersion relations predicted by the FE simulation based on the exact microstructure and the experimental measurement are also plotted in the figure. The band gap for the lowest symmetric guided wave can be found in the frequency range of 17.7–22.8 kHz, which has very good agreement with that from the experimental results. For the lowest antisymmetric guided wave and the shear horizontal wave, excellent agreement between the predictions of the current model and the exact FE simulation is found at low-frequency range but there is a small discrepancy at the higher-frequency regime.

To understand wave behavior of different guided wave modes in the EMM plate, a guided wave propagating along a 45° with respect to the principal x_1 direction is studied. In the example, to demonstrate an engineering application of the metamaterial plate in the low-frequency band-gap range, the rubber-coated lead cores are embedded in the epoxy matrix, with material properties for lead ($\rho_C = 11310\,\text{kg/m}^3$, $E_C = 13\,\text{GPa}$, $\nu_C = 0.435$), epoxy
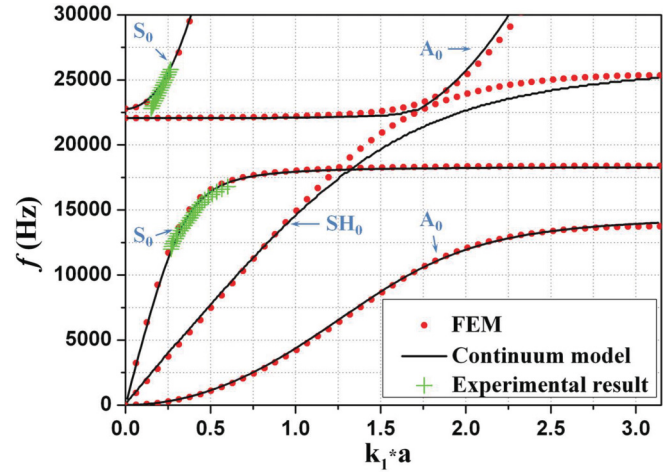

FIG. 13. (Color online) Comparison of the dispersion curves obtained by the continuum model, FE simulation, and experimental measurement for the guided wave along the principal x_1 direction.

($\rho_M = 1110\,\text{kg/m}^3$, $E_M = 4.4\,\text{GPa}$, $\nu_M = 0.38$) and rubber ($\rho_{CT} = 1300\,\text{kg/m}^3$, $E_{CT} = 10\,\text{MPa}$, $\nu_{CT} = 0.499$); the geometrical parameters of the microstructure are the same as those in Table I. The anisotropic effective mass density tensor and the effective stiffness matrix are similarly obtained by using the numerically based effective medium model. Figure 14(a) shows the comparison of dispersion relations in the first Brillouin zone from the continuum model and the numerical simulation based on the exact microstructure, where ω_0 is the locally resonant angular frequency of the microstructure along the x_1 direction and $k^* = (k_1a + k_2a)/2$. Excellent agreement can be observed in the two lowest-order modes because the coupling of the different wave modes does not occur.

More complicated wave repulsions can be observed in the high-order wave mode diagram from the dispersion prediction by the exact numerical simulation; however, they cannot be predicted by the current continuum model. To give more intuitive understanding of the wave repulsion, the displacement fields of eigenmodes at several gap-edge frequencies marked in Fig. 14(a) (points 1–10) are plotted in Fig. 14(b) to show the physical mechanism of the wave repulsion. From Fig. 14(b), it can be found that the dispersion curve containing points 1, 7, and 9, which can also be predicted by the continuum model, describes the out-of-plane dominant motion. The wave repulsion, which is reflected at points 2 and 6, is caused by the local rotation resonance (x-z plane) in the core. Therefore, it is understandable that the continuum model cannot capture this motion. As a result of the repulsion, the mode coupling can also be observed. For example, the displacement field in the lowest antisymmetric guided wave mode is dominated by the out-of-plane plate motion, as shown in Fig. 14(b1), below the local rotation resonant frequency which is dominated by a coupling motion between the plate motion and local resonance motion above the local rotation resonant frequency, as shown in Figs. 14(b7) and 14(b9). An additional flat band is found from the exact numerical simulation, which cannot be reflected from the continuum model at the frequency $\omega/\omega_0 = 1.6$. From the displacement fields at points 3 and 8, it can be found that the narrow passing band is caused by the local rotation resonance

TABLE II. Effective stiffness matrix of the EMM plate (in GPa).

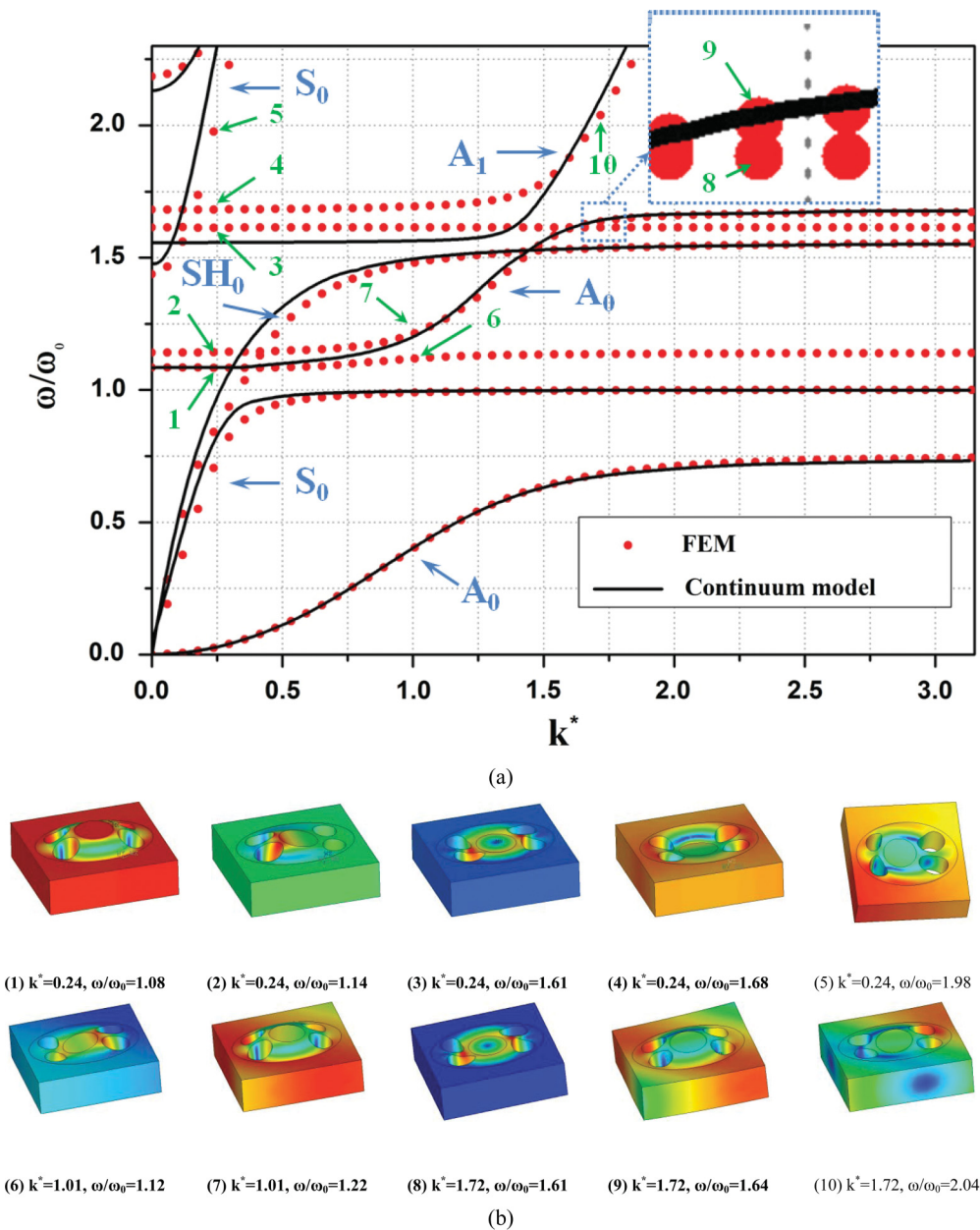| C_{11}	C_{12}	C_{13}	C_{22}	C_{23}	C_{33}	C_{44}	C_{55}	C_{66}
36.64	5.57	13.53	18.83	7.84	48.38	12.41	6.69	2.272

FIG. 14. (Color online) (a) Comparison of the dispersion curves obtained by the continuum model and the FE simulation for the guided wave propagation along $45°$ with respect to the principal x_1 direction; (b) the displacement fields around several gap-edge modes in points 1–10.

(x-y plane) in the coating medium, which cannot be captured by the current continuum model. The difference between the current model and the exact numerical simulation is found for the high-order wave modes; the corresponding displacement fields are plotted in Fig. 14(b) at points 4, 5, and 10. From the displacement fields at points 4, 5, and 10, it can be seen that the high-order wave modes are also the coupling modes of the plate motions and local rotation resonant motion. Therefore, the difference between the two models is due to the coupling behavior, which cannot be captured by the continuum model.

Based on the developed continuum model, we will further study the wave behavior of the anisotropic EMM plate, such as existence of preferential directions of effective velocities and energy flow. Figures 15(a) and 15(b) show the slowness curves of both symmetric and antisymmetric waves in the

metamaterial plate at three different frequencies, respectively. In the figures, ω_0 is the locally resonant angular frequency of the microstructure along the x_1 direction, $c_T^0 = \sqrt{C_{66}/\rho^0}$ is the in-plane bulk transverse wave velocity, and ρ^0 is the static mass density of the plate. In the example, the microstructure design proposed in Fig. 3(a) is chosen with lead, rubber, and epoxy as the core, coating, and matrix materials, respectively. From Fig. 15(a), we notice that the anisotropy of effective velocities is obvious; the effective velocity along the x_1 direction is higher than that along the x_2 direction. For the frequencies at $\omega/\omega_0 = 0.14$ and 0.7, the shapes of the slowness curves indicate strong energy focusing along specific x_1 and x_2 directions. For the frequency at $\omega/\omega_0 = 2.0$, the anisotropy increases and most energy will propagate along the x_1 direction. However, for the antisymmetric wave, as shown in Fig. 15(b), few changes in the

(a) Symmetric wave
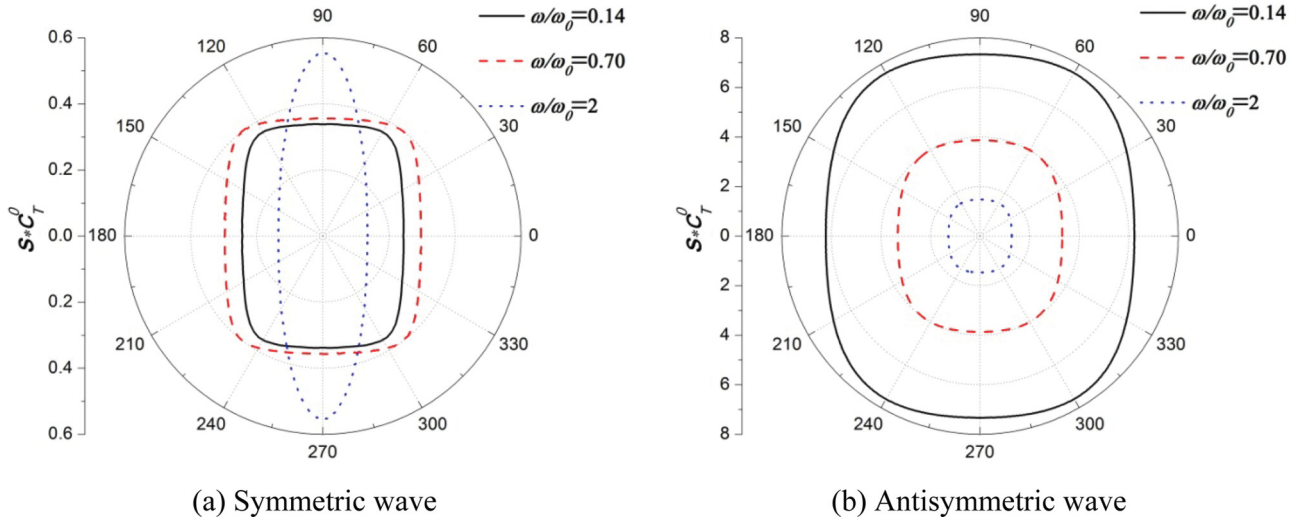
(b) Antisymmetric wave

FIG. 15. (Color online) Slowness curves of symmetric and antisymmetric wave at different frequencies.

shapes of slowness curves can be found at the three different frequencies.

In order to further evaluate the difference between the phase direction and energy direction quantitatively at different frequencies, the energy flow direction as a function of phase direction angle is plotted in Fig. 16. For simplicity but without loss of generality, we assume that the guided wave is propagating along the x axis which has an angle δ with respect to the principal x_1 axis and $\theta = \tan^{-1}(\frac{\partial \omega / \partial k_y}{\partial \omega / \partial k_x})$ is the difference between the group velocity direction and the phase velocity direction. It can be noticed that the relation between the directions of phase velocity and group velocity is almost invariable for the antisymmetric wave at different frequencies, which explains the consistency of the shapes of the slowness curves in Fig. 15(b). In contrast with the results of the antisymmetric wave, the relations between the directions of phase velocity and group velocity for different symmetric wave modes change obviously at different frequencies in Fig. 16, which is also

consistent with the result shown in Fig. 15(a). It should also be noticed that except for the two principal directions, the zero value of θ, which represents that the energy propagation direction is parallel to the phase direction, also occurs when the first symmetric wave (black circle and red triangle) propagates along the direction that deviates at 50° to 60° from the principal x_1 axis. However, no energy flow propagates parallel to the phase direction when the propagation direction of the second symmetric wave mode (blue square) does not coincide with either principal direction of the EMM plate.

V. CONCLUSION

This paper presented a microstructure design and conducted an experimental validation of wave propagation in an EMM plate with anisotropic effective mass density. The design was achieved via a numerically based effective medium model. The experimental validation was conducted in the EMM plate through the analysis of the harmonic and transient wave propagation. The group and phase velocities as functions of frequency were obtained from transmission measurements of the transient wave signals with the aid of the wavelet technology, from which the effective mass densities along the two principal directions of the proposed EMM plate were then experimentally demonstrated. Excellent agreements between the experimental results and those from the numerically based effective medium model were observed. Finally, a continuum model of guided wave propagation in the anisotropic EMM plate has been developed. The continuum model can correctly predict different guided wave modes in the EMM plate, which are difficult to measure experimentally. Particularly, the high-order guided wave coupling and repulsion as well as the preferential energy flow direction in the anisotropic EMM plate were discussed.
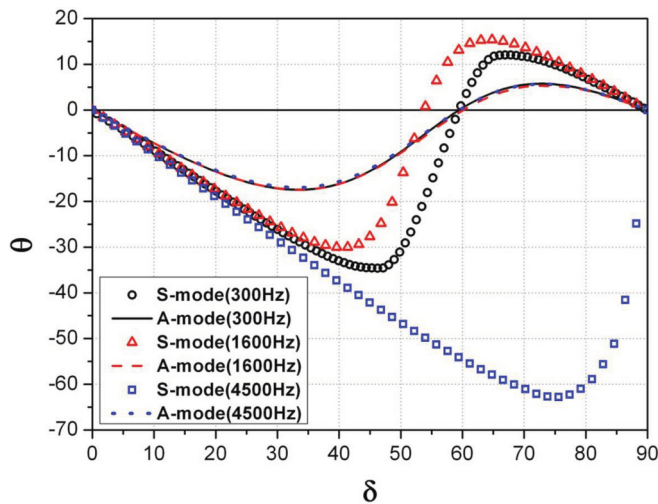
FIG. 16. (Color online) Energy direction θ with respect to the phase direction δ for symmetric and antisymmetric wave propagations at various frequencies.

*Corresponding author: glhuang@ualr.edu

[1] Z. Liu, X. Zhang, Y. Mao, Y. Y. Zhu, Z. Yang, C. T. Chan, and P. Sheng, Science **289**, 1734 (2000).

[2] X. Hu, C. T. Chan, and J. Zi, Phys. Rev. E **71**, 055601 (2005).

[3] N. Fang, D. Xi, J. Xu, M. Ambati, W. Srituravanich, C. Sun, and X. Zhang, Nat. Mater. **5**, 452 (2006).

[4] P. F. Pai, J. Intell. Mater. Syst. Struct. **21**, 517 (2010).

[5] D. Torrent and J. Sánchez-Dehesa, New J. Phys. **9**, 323 (2007).

[6] S. Zhang, L. L. Yin, and N. Fang, Phys. Rev. Lett. **102**, 194301 (2009).

[7] S. Gonella, A. C. To, and W. K. Liu, J. Mech. Phys. Solids **57**, 621 (2009).

[8] A. P. Liu, R. Zhu, X. N. Liu, G. K. Hu, and G. L. Huang, Wave Motion **49**, 411 (2012).

[9] S. A. Cummer and D. Schurig, New J. Phys. **9**, 45 (2007).

[10] M. Schoenberg and P. N. Sen, J. Acoust. Soc. Am. **73**, 61 (1983).

[11] Y. Cheng, F. Yang, J. Y. Xu, and X. J. Liu, Appl. Phys. Lett. **92**, 151913 (2008).

[12] D. Torrent and J. Sánchez-Dehesa, Phys. Rev. Lett. **103**, 064301 (2009).

[13] D. Torrent and J. Sánchez-Dehesa, New J. Phys. **10**, 023004 (2008).

[14] J. B. Pendry and J. Li, New J. Phys. **10**, 115032 (2008).

[15] L. Zigoneanu, B. I. Popa, and S. A. Cummer, J. Appl. Phys. **109**, 054906 (2011).

[16] Z. Liu, C. T. Chan, and P. Sheng, Phys. Rev. B **71**, 014103 (2005).

[17] G. W. Milton and J. R. Willis, Proc. R. Soc. A **463**, 855 (2007).

[18] G. W. Milton, New J. Phys. **9**, 359 (2007).

[19] P. Sheng, X. X. Zhang, Z. Y. Liu, and C. T. Chan, Physica B **338**, 201 (2003).

[20] Y. Gu, X. Luo, and H. Ma, J. Appl. Phys. **105**, 044903 (2009).

[21] H. H. Huang and C. T. Sun, Philos. Mag. **91**, 981 (2011).

[22] Y. Wu, Y. Lai, and Z. Q. Zhang, Phys. Rev. Lett. **107**, 105506 (2011).

[23] Y. Lai, Y. Wu, P. Sheng, and Z. Q. Zhang, Nat. Mater. **10**, 620 (2011).

[24] X. M. Zhou and G. K. Hu, Phys. Rev. B **79**, 195109 (2009).

[25] X. N. Liu, G. K. Hu, C. T. Sun, and G. L. Huang, J. Sound Vib. **330**, 2536 (2011).

[26] M. Hirsekorn and P. P. Delsanto, J. Appl. Phys. **99**, 124912 (2006).

[27] S. Nemat-Nasser, J. R. Willis, A. Srivastava, and A. V. Amirkhizi, Phys. Rev. B **83**, 104103 (2011).

[28] F. Song, G. L. Huang, and K. Hudson, Smart Mater. Struct. **18**, 125007 (2009).

[29] M. Sato, J. Acoust. Soc. Jpn. **47**, 405 (1991).